ADVANCED MATERIALS
www.advmat.de

Stacking-Controlled Growth of rBN Crystalline Films with High Nonlinear Optical Conversion Efficiency up to 1%

Jiajie Qi, Chenjun Ma, Quanlin Guo, Chaojie Ma, Zhibin Zhang, Fang Liu, Xuping Shi, Li Wang, Mingshan Xue, Muhong Wu, Peng Gao, Hao Hong, Xinqiang Wang, Enge Wang, Can Liu, and Kaihui Liu**

Nonlinear optical crystals lie at the core of ultrafast laser science and quantum communication technology. The emergence of 2D materials provides a revolutionary potential for nonlinear optical crystals due to their exceptionally high nonlinear coefficients. However, uncontrolled stacking orders generally induce the destructive nonlinear response due to the optical phase deviation in different 2D layers. Therefore, conversion efficiency of 2D nonlinear crystals is typically limited to less than 0.01% (far below the practical criterion of >1%). Here, crystalline films of rhombohedral boron nitride (rBN) with parallel stacked layers are controllably synthesized. This success is realized by the utilization of vicinal FeNi (111) single crystal, where both the unidirectional arrangement of BN grains into a single-crystal monolayer and the continuous precipitation of (B,N) source for thick layers are guaranteed. The preserved in-plane inversion asymmetry in rBN films keeps the in-phase second-harmonic generation field in every layer and leads to a record-high conversion efficiency of 1% in the whole family of 2D materials within the coherence thickness of only 1.6 µm. The work provides a route for designing ultrathin nonlinear optical crystals from 2D materials, and will promote the on-demand fabrication of integrated photonic and compact quantum optical devices.

1. Introduction

2D boron nitride (BN), with broad spectrum transparency (optical bandgap of ≈6 eV),[1,2] large nonlinear coefficient $\chi^{(2)}$ (ranging from 10 to 40 pm V^{-1}),[3–8] excellent physicochemical stability (steady at 1500 °C in air),[9] and laser damage threshold (theoretically of 7.95 TW cm^{-2} under 1600 nm femtosecond pulsed laser excitation),[10] has been regarded as a promising candidate for ultrathin nonlinear optical crystals.[11–13] However, the absolute light–matter interaction for BN monolayer is too weak (the typical conversion efficiency is below 10^{-9}), due to the limited interaction length of only one atomic-layer thickness. Among numerous engineering methods,[14–16] increasing the number of BN layers is definitely able to strengthen the light–matter interaction. While for the universal bulk BN crystals of hexagonal phase (hBN), the adjacent layers follow the 180°-rotated stacking sequence, where the restored inversion

J. Qi, C. Ma, Q. Guo, C. Ma, Z. Zhang, F. Liu, X. Shi, H. Hong, X. Wang, K. Liu
State Key Laboratory for Mesoscopic Physics
Frontiers Science Center for Nano-Optoelectronics
School of Physics
Peking University
Beijing 100871, China
E-mail: khliu@pku.edu.cn

L. Wang, E. Wang
Beijing National Laboratory for Condensed Matter Physics
Institute of Physics
Chinese Academy of Sciences
Beijing 100190, China

M. Xue
School of Materials Science and Engineering
Nanchang Hangkong University
Nanchang 330063, China

M. Wu, P. Gao, E. Wang, K. Liu
International Center for Quantum Materials
Collaborative Innovation Center of Quantum Matter
Peking University
Beijing 100871, China

E. Wang, K. Liu
Songshan Lake Materials Lab
Institute of Physics
Chinese Academy of Sciences
Dongguan 523808, China

C. Liu
Key Laboratory of Quantum State Construction and Manipulation
(Ministry of Education)
Department of Physics
Renmin University of China
Beijing 100872, China
E-mail: canliu@ruc.edu.cn

The ORCID identification number(s) for the author(s) of this article can be found under https://doi.org/10.1002/adma.202303122

DOI: 10.1002/adma.202303122

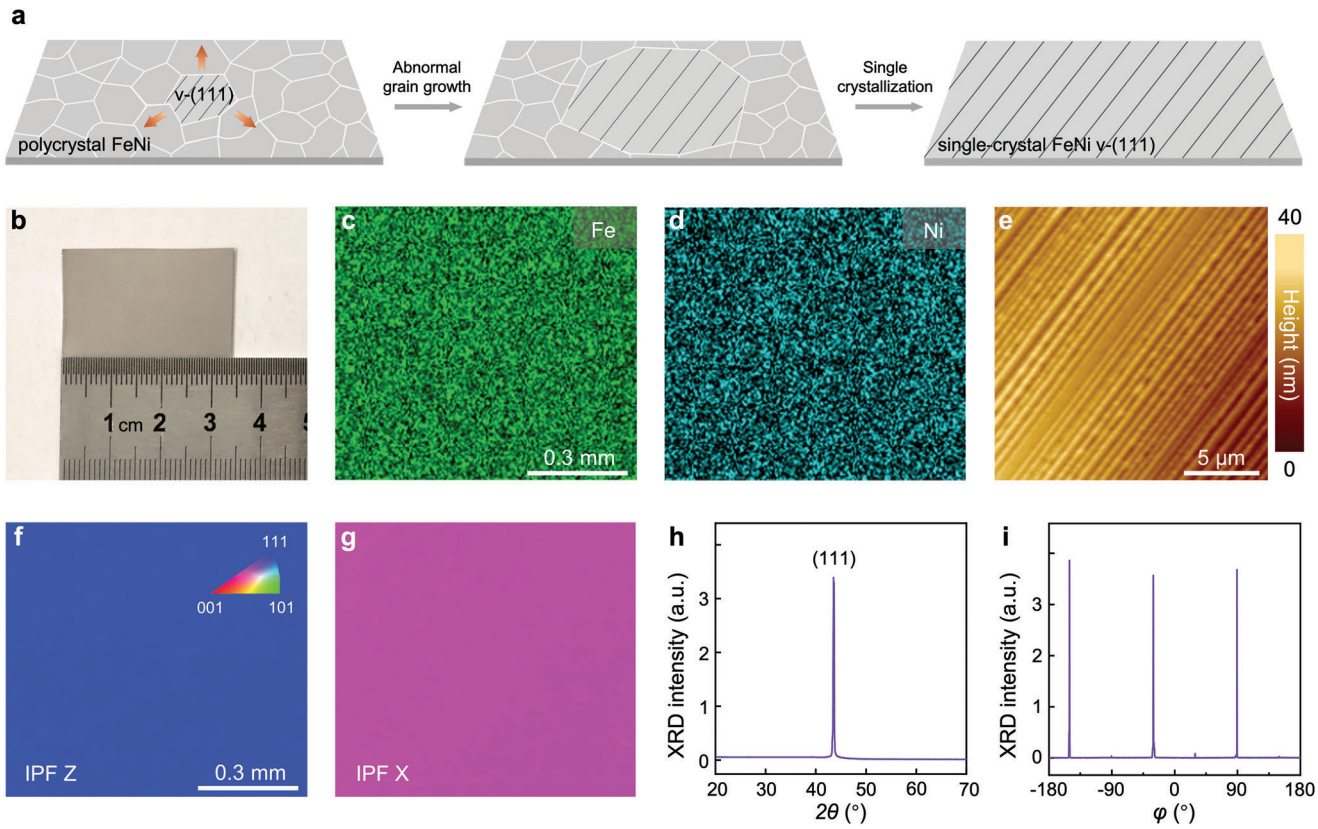

Figure 1. Characterizations of single-crystal FeNi v-(111) alloy. a) Schematic of the seeded abnormal grain growth of FeNi v-(111) single crystal by a high-temperature annealing method. b) Photograph of the single-crystal FeNi v-(111) foil. c,d) In-plane EDS mappings of Fe (c) and Ni (d), respectively, indicating the even distribution of two compositions. e) AFM mapping of the area with parallel steps on as-obtained FeNi v-(111) surface. f,g) EBSD IPF mappings along the *Z* (f) and *X* (g) directions, respectively. The two images are of the same size. h,i) XRD 2θ-scan pattern (h) and φ-scan data corresponding to FeNi (100) (i), respectively, confirming the single-crystal nature of the FeNi v-(111) foil without in-plane rotation.

symmetry gives rise to a quenched nonlinear optical response between adjacent layers.[3,4] In contrast, rhombohedral BN (rBN) thick crystals, in which each atomic layer is stacked in parallel to maintain the same in-plane dipole orientation, naturally satisfy the coherent enhancement condition of nonlinear optical signals. Hence, the stacking-controlled growth of rBN thick crystals is an essential prerequisite for harnessing versatile and efficient nonlinear optical processes, as well as for facilitating compact integrated photonic applications.

In contrast to the success in wafer-scale production of single-crystal BN monolayers and few layers,[17–20] the growth of thick rBN can be achieved only in a narrow experimental window and the preparation status is stuck in nanosheets or bulk flakes mixed with hexagonal and turbostratic phases.[21–23] The quite low solubility of B or/and N in epitaxial substrates (Cu, Ni, Pt, Ru, etc.) usually dominates the self-limited growth and therefore restricts the formation of adlayers for a thick crystal.[24–28] Recently, great progress has been made to tackle this limitation, notably the development of dissolution-precipitation growth strategies, e.g., the vapor–liquid–solid synthesis method and metal solvent-assisted approaches.[29–34] The thickness of as-synthesized BN film is remarkably increased, ranging from tens of nanometers to micrometers. However, the absence of surface or/and interface modulations in these molten-substrate-based methods makes the arrangement of BN layers governed by the weak van der Waals interaction, resulting that the major component is routinely of the most thermodynamically stable hBN.[35,36] Thus, exploiting accessible techniques to simultaneously achieve adequate supply of (B, N) source and the effective modulation of stacking order is paramount for obtaining large-sized thick rBN crystal.

In this work, we propose a stacking-controlled continuous precipitation strategy to synthesize uniform rBN crystalline films (lateral size of 2×1 cm^2 and thickness >1 μm) on the vicinal surface of single-crystal FeNi (111) foil. The presence of parallel steps on the FeNi surface guides BN grains to be seamlessly stitched into a single-crystal monolayer, and the continuous dissolution and precipitation of (B, N) sources in FeNi further ensure those monolayers to be stacked in a parallel sequence for rBN thick layers. The unidirectional in-plane polar dipoles along the armchair direction in each BN monolayer, together with parallel stacking structure in adjacent layers, contribute to the coherent enhancement of nonlinear optical signals. Moreover, the off-resonant excitation capability of rBN, which is undisturbed in the ultraviolet (UV) and visible (vis) spectral range due to its large bandgap, allows the rBN crystalline film to exhibit a higher laser-induced damage threshold of ≈200 GW cm^{-2} compared to other reported 2D nonlinear materials. Consequently, a high absolute second-harmonic generation (SHG) efficiency up to 1% was feasibly

accessible within this well-stacked rBN crystalline film with the coherence thickness of 1.6 μm. This work highlights the immense potential of rBN as an ultrathin nonlinear optical crystal over a broad spectral transparency window and lays the groundwork for advancing 2D-material-based ultrafast and high-power lasers, photonic integrated circuits, and quantum light sources.

2. Results and Discussion

2.1. Preparation of Vicinal FeNi (111) Single Crystal

In our growth strategy, the utilization of FeNi foil is a key for the precipitation of rBN thick layers, because: i) the dissolution of both B (through reaction-diffusion with Fe and Ni) and N (solubility of ≈8 at% at 1000 °C in Fe) atoms enables to be significantly increased in FeNi alloys;[30] ii) the introduction of Ni atoms can effectively prevent the phase transition of pure Fe and guarantee the formation of large-scale FeNi single crystals;[37] iii) the parallel steps on solid FeNi surface are capable to manipulate the stacking configuration of BN crystalline films.

Based on the seeded abnormal grain growth mechanism,[38] centimeter-scale single-crystal FeNi with (111) vicinal surface (we name as v-(111) below if not specified) was prepared by annealing a commercial polycrystalline Permalloy foil (60 wt% Fe) at 1450 °C near the molten point (**Figure 1**a,b, and the Experimental Section). Parallel steps existing on the FeNi v-(111) was steadily extended along with the grain enlargement, which was further demonstrated by the atomic force microscopy (AFM) image (Figure 1e) after cooling down to the room temperature. Figure 1c,d showed the uniform in-plane energy-dispersive spectroscopy(EDS) mappings of Fe and Ni, respectively, indicating that both components were evenly distributed without phase separation. For investigating the FeNi alloy crystallography, electron backscatter diffraction (EBSD), and X-ray diffraction (XRD) measurements were specifically conducted. As shown in Figure 1f, the uniform color in EBSD inverse pole figure (IPF) mapping along the *Z* direction verified that the whole FeNi alloy possessed the same v-(111) surface; meanwhile, the IPF mapping along the *X* direction affirmed the v-(111) surface without any in-plane rotation (Figure 1g). Furthermore, the sharp (111) peak in the XRD 2θ-scan pattern (Figure 1h) and the presence of only three peaks at an interval of exactly 120° in the φ-scan data (Figure 1i), unambiguously confirmed the single-crystal nature of large-scale FeNi v-(111) substrate.

2.2. Stacking-Controlled Growth of rBN Crystalline Film

In the rBN crystalline film growth, the preannealed single-crystal FeNi v-(111) substrate was tightly placed onto a piece of hot-pressed BN paper (**Figure 2**a). At elevated temperatures, the (B,N) sources from the paper would incessantly dissolve into the one-side surface, diffuse through the whole metal and finally precipitate at the opposite surface of the FeNi foil, where the growth process is similar with that of single-crystal graphite film.[39] When the (B,N) source precipitated from the FeNi foil, the atomic steps on v-(111) surface would guide them to form unidirectionally aligned BN domains and seamlessly stitch together to create the single-crystal BN monolayer. Then, the subsequent BN layers were precipitated with the same grain orientation as the first layer under the same step-controlled condition, and stacked in parallel to obtain the rBN thick layers. After 40 h of growth, a homogenous rBN thick film was formed on the FeNi v-(111) surface with a typical lateral size of 2×1 cm^2 (Figure 2b). The thickness of BN film was evaluated to be ≈1.2 μm as shown in the cross-sectional scanning electron microscopy (SEM) image, in which the insulating BN showed a brighter contrast than that of conductive FeNi substrate (Figure 2c; and Figure S1, Supporting Information). Meanwhile, the precipitated thickness showed a linear dependence on the growth time with an estimated rate of about 30 nm h^{-1} (Figure S2, Supporting Information).

Additionally, due to the different coefficients of thermal expansion of BN film and metal foil,[40] the as-grown rBN layers would shrink and form wrinkles during the cooling process. The high crystallinity of rBN films with in-plane threefold symmetry can be directly inferred from the observed wrinkles (Figure 2d), which are oriented along three main directions with a relative angle of 60°. Figure 2e showed that rBN crystalline films can be intactly transferred onto the fused silica and exhibit high optical transparency. The intrinsic bandgap of rBN film was further identified to be ≈5.8 eV by UV–vis absorption spectroscopy (Figure 2f) and the corresponding Tauc plot of $(\alpha E)^{1/2}$ vs E (Figure S3a, Supporting Information). Here α and E represent the optical absorption coefficient and the photon energy, respectively, and the usage of exponent 1/2 is due to the indirect bandgap property of rBN crystals.[41] This large bandgap guarantees that our BN films are capable to achieve nonlinear frequency conversion over a wide spectral range without the absorption of generated signals. The pronounced (003) and (006) peaks in the XRD 2θ-scan data confirmed that the as-grown BN film was well aligned along the out-of-plane direction perpendicular to the substrate (Figure 2g). Additionally, in X-ray photoelectron spectroscopy (XPS) measurements, the sharp characteristic peaks of B 1s and N 1s indicated that a pristine BN film has been obtained (Figure S3b, Supporting Information). Figure 2h illustrated the characteristic Raman E_{2g} peak of rBN crystals at 1365 cm^{-1} with a narrow full width at half maximum (FWHM) of ≈9 cm^{-1}, which verified the high crystalline quality.

2.3. Confirmation of Interlayer Stacking Sequence of rBN Crystalline Film

As illustrated in **Figure 3**a, there are generally two types of stable configurations for BN thick layers.[36] In the hBN phase, hexagons are aligned, but adjacent layers are rotated by 180° relative to each other (right panel in Figure 3a). This arrangement is referred to as the AA′A stacking order with the restored inversion symmetry. In contrast, the rBN phase exhibits the ABC stacking sequence and consists of BN layers successively translating in the same direction by the interatomic distance (left panel in Figure 3a). This configuration preserves the in-plane inversion asymmetry inherently in the BN monolayer. And the two distinct interlayer stacking sequence of hBN and rBN will result in destructive and constructive nonlinear optical responses (discussed in further detail later), respectively. As evidenced that the rBN crystal exhibited a six-fold polarized SHG pattern with an intensity of five orders of magnitude stronger than that of the

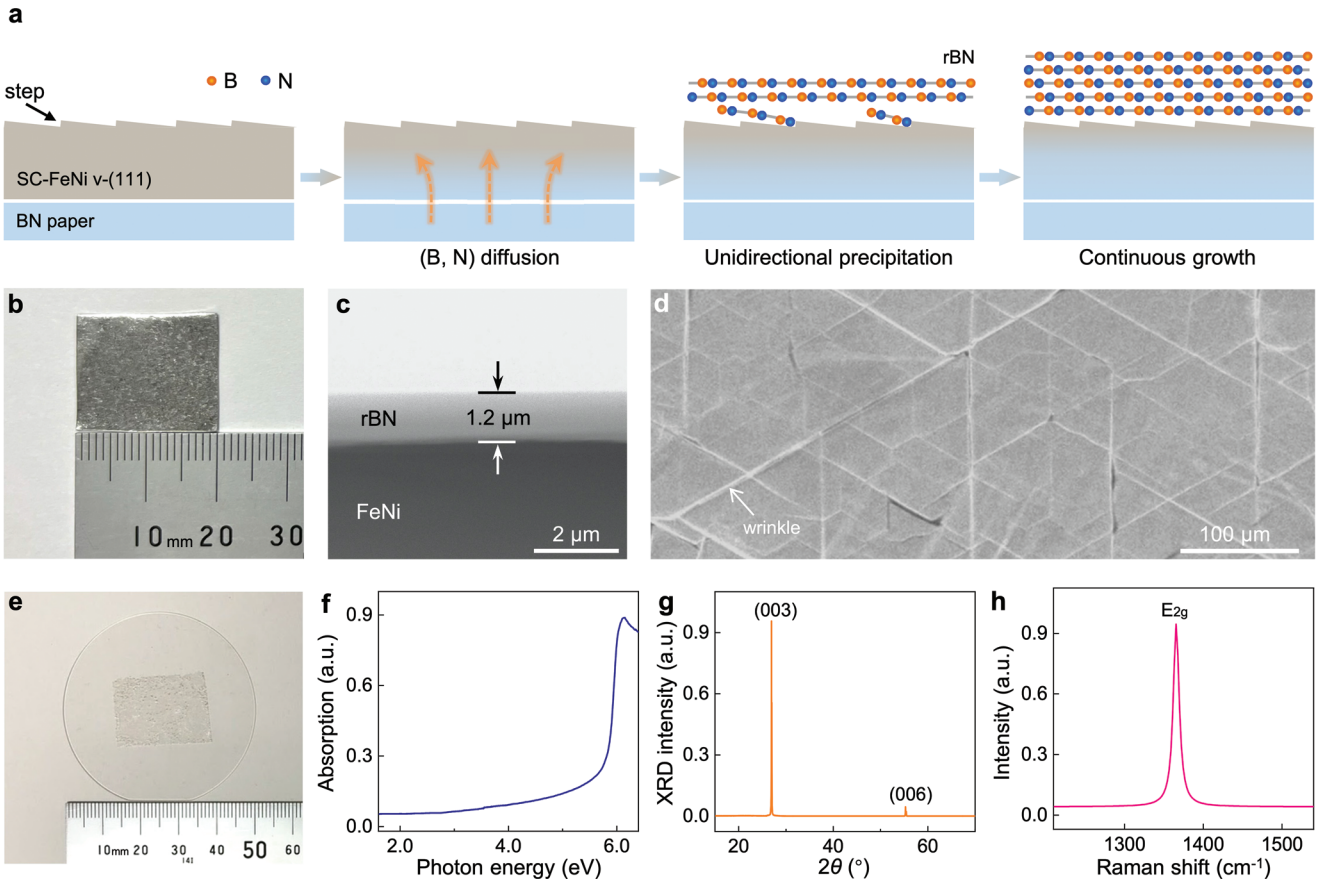

Figure 2. Growth and characterizations of rBN crystalline films. a) Schematic of the stacking-controlled continuous precipitation strategy, in which the orange and blue balls represent the boron and nitrogen atoms, respectively, and SC means single-crystal. b) Photograph of an as-grown rBN film on the FeNi v-(111) single crystal. c,d) Cross-sectional (c) and planar (d) SEM images of the rBN film with thickness of 1.2 μm, respectively. e) Photograph of a transferred rBN film on a fused silica wafer. f) UV–vis absorption spectrum of the transferred rBN film, showing an optical bandgap of ≈5.8 eV. g) XRD 2θ-scan data of the transferred rBN film, indicating that the rBN layers are well aligned along the out-of-plane direction. h) Raman spectrum of the rBN film. The FWHM of the Raman E_{2g} mode is measured to be ≈9.0 cm^{-1}.

commercial hBN flakes at a same thickness of ≈40 nm (Figure 3b). Three main peaks at intervals of exactly 120° in the XRD φ-scan data (Figure 3c) indicated that the as-grown rBN crystalline film predominantly followed the ABC stacking order due to its $R3m$ symmetry. Otherwise, there would be six peaks with identical intervals of 60° in the XRD φ-scan for both hBN crystals and twinned rBN crystals.[22]

To further verify the stacking sequence of the as-grown rBN, high-resolution transmission electron microscopy (HRTEM) was employed to visualize its atom arrangement. As depicted in Figure 3d, the equal-contrast triangular lattice with the lattice constant of 0.252 nm along the a-axis was a strong signature of the ABC stacking structure. Simultaneously, the first-order to second-order peak intensity ratio was near zero in the selected-area electron diffraction (SAED) pattern (Figure 3e), which has also been widely utilized to figure out the rBN crystalline morphology.[42] Furthermore, the cross-sectional scanning transmission electron microscopy (STEM) image of rBN clearly demonstrated that each layer slid along the same direction through the single B–N bond distance, providing direct evidence of the parallel ABC stacking configuration (Figure 3f). The 2θ peak position of ≈26.72° in high-resolution XRD (0.12% smaller than that of hBN) (Figure 3g) was consistent with the interlayer distance of 0.333 nm. We also occasionally observe the ABA-stacking (Bernal) phase, wherein the BN layers are stacked in parallel but the periodicity is only two layers instead of three layers found in ABC-stacking phase. Actually, both two phases contribute equally to the in-plane nonlinear optical response.

2.4. High-Efficiency SHG Response of rBN Crystalline Film

To qualitatively understand the stacking-determined nonlinear optical response as mentioned above, we illustrate the layer-dependent SHG in both rBN and hBN thick crystals. In the case of hBN, the 180°-rotated stacking order results in antiparallel orientations of second-order nonlinear polarization $\boldsymbol{P}(2\omega)$ in adjacent layers (**Figure 4**b, right panel). This causes the SHG intensity ($I(2\omega)$) to destructively interfere with one another, leading to $I(2\omega)$ tending to be zero in hBN crystals with even number of layers. In contrast, for rBN crystals, the parallel stacking structure ensures unidirectional alignment of each $\boldsymbol{P}(2\omega)$, which

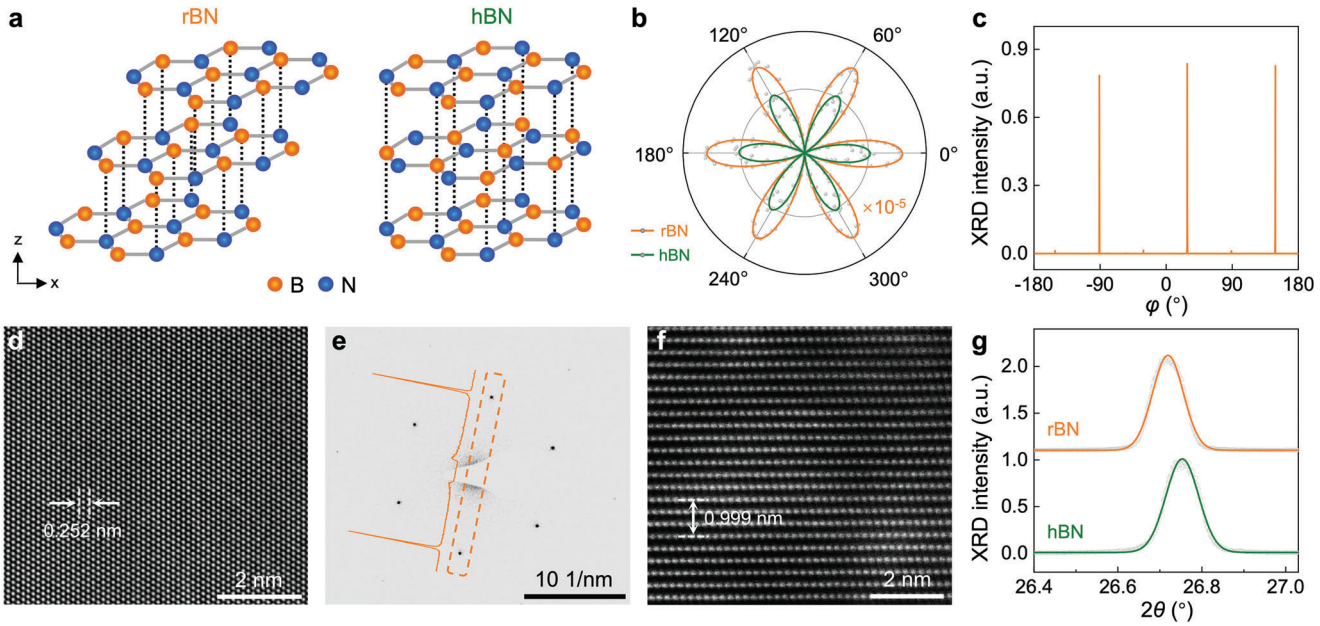

Figure 3. Confirmation of interlayer stacking configuration for the crystalline rBN film. a) Schematics of the stacking configuration of rBN (left) and hBN (right). b) Polarized SHG patterns for as-grown rBN and commercial hBN flakes. The two exfoliated flakes have the similar thickness of ≈40 nm, while the SHG intensity of rBN is five orders of magnitude stronger. c) XRD φ-scan pattern of rBN film. The three main peaks at an identical interval of exactly 120° corresponding to rBN (102) indicate the threefold rotation symmetry of the rBN crystalline film. d,e) Planar HRTEM image (d) and the corresponding SAED pattern (e) of the rBN, respectively. The same triangular lattice contrast is visualized, and the lattice constant along *a*-axis is measured as 0.252 nm in (d). The orange line in (e) is the intensity profile. The result that the ratio of the first-order to second-order diffraction spots is almost zero confirms the ABC stacking sequence of the crystalline rBN film. f) Cross-sectional atomic-resolution STEM image of the rBN film with an interlayer distance of 0.333 nm. g) High-resolution XRD 2θ-scan spectra of two kinds of BN film. The smaller peak position of as-grown rBN film shows a larger interlayer distance (about 0.12%) than that of the hBN counterpart.

facilitates constructive interference of the second-harmonic electric field and coherent enhancement of $I(2\omega)$ as rBN's thickness (T) increases (Figure 4b, left panel). Quantitatively, the thickness dependence of $I(2\omega)$ can be calculated as below (more details in Note S1, Supporting Information)

$$I(2\omega) = \frac{4\omega^2}{c^3\varepsilon_0 n^2(\omega)\, n(2\omega)} \left(\chi^{(2)}\right)^2 I^2(\omega)\, T^2 \frac{\sin^2(\Delta k \cdot T/2)}{(\Delta k \cdot T/2)^2} \quad (1)$$

where $\chi^{(2)}$ represents the second-order nonlinear coefficient of rBN films and is measured to be 30 pm V^{-1} using the d_{22} of $LiNbO_3$ as reference (Figure S4, Supporting Information). Δk is the wavevector mismatch for SHG, which can be obtained from the light wavelength (λ) and refractive index (n) of fundamental (ω) and second-harmonic (2ω) waves. The speed of light and the dielectric constant in vacuum are denoted by c and ϵ_0, respectively.

Then an optical transmission geometry (Figure 4a) was utilized to systematically measure the SHG response of the as-prepared rBN films with 800 nm femtosecond pulsed laser excitation (the excitation wavelength was fixed at 800 nm if not specified). As shown in Figure 4c, the SHG signal exhibited a quadratic dependence on thickness when rBN films were negligibly thin ($\Delta k \cdot T \to 0$), as described in Equation (1). However, as the rBN crystal incessantly thickened, where $\Delta k \cdot T$ cannot be ignored, the squared increase in SHG intensity was disrupted, and the signal transitioned to a sinusoidal response and even declined when the rBN thickness exceeded ≈1.6 µm (Figure 4d). This optical response is referred to as the phase-mismatching effect. The underlying cause for this effect is the discrepancy in the refractive indices of the fundamental ($n(\omega)$) and second-harmonic ($n(2\omega)$) waves propagating through the thick rBN layers,[43] resulting in a wavevector mismatch, calculated as $\Delta k = k(2\omega) - 2k(\omega) = \frac{4\pi}{\lambda(\omega)} \cdot (n(2\omega) - n(\omega))$. Under the condition of $\Delta k \cdot T = \pi$, the SHG intensity reached its maximum (≈10^7 times higher than that of the monolayer, as determined in Figure 4e). The featural coherence thickness (l_c) can be derived as $l_c = \frac{\lambda(\omega)}{4|n(\omega)-n(2\omega)|} \approx 1.6$ µm, which was well consistent with our experimental results.

Besides that, the SHG conversion efficiency, denoted by $\eta_{SHG} \propto I(2\omega)/I(\omega)$, is directly proportional to the pump intensity $I(\omega)$, as determined by Equation (1). It implies that one can continuously enhance the conversion efficiency by employing higher-power excitation until the materials are damaged by the pump laser (at which point the maximum tolerable laser power is referred to as the damage threshold). Benefiting from the large bandgap, rBN crystal potentially avoids resonant excitation of states at the band edge and shallow defects, resulting in high laser-induced damage threshold and high transparency of the generated second-harmonic waves. Figure 4f presented the excitation-power-dependent SHG response, indicating a damage threshold of ≈200 GW cm^{-2} at the thickness of l_c (Note S2, Supporting Information), which was similar with that of the monolayer. Under the highest-power circularly polarized pump, a conversion efficiency up to ≈1% was achieved, which closely aligned with the theoretical estimation of ≈1.7%, with the visible SHG output of

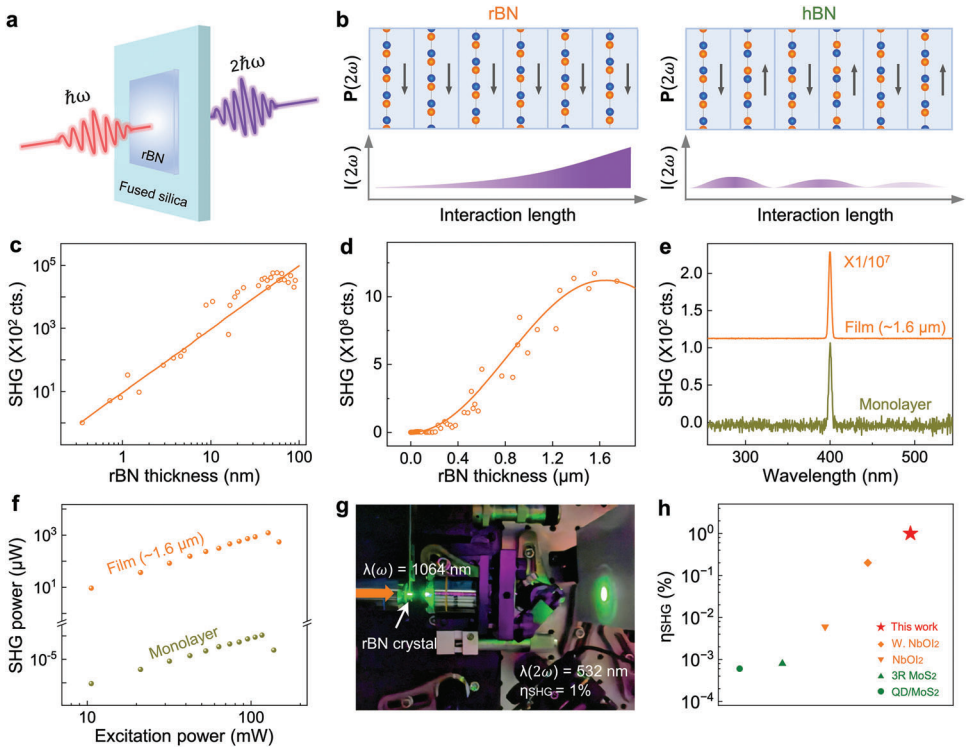

Figure 4. High-efficiency SHG in the rBN crystalline films. a) Schematic illustration of the SHG response of rBN films in an optical transmission geometry. b) Detailed schematics of the enhanced and vanishing SHG in rBN and hBN films, respectively. The black arrow represents the in-plane second-order nonlinear polarization ($\boldsymbol{P}(2\omega)$), and $I(2\omega)$ means the SHG intensity. Aligned $\boldsymbol{P}(2\omega)$ in rBN accounts for the coherently enhanced SHG while the antiparallel $\boldsymbol{P}(2\omega)$ in hBN makes the SHG signals cancel with each other. c,d) Thickness-dependent SHG of rBN films, where dots and curves are the experimental and simulated results, respectively. The SHG intensity shows an expected quadratic law within a thin thickness of ≈100 nm (c), and undergoes a sinusoidal response when the thickness exceeds the coherence length of l_c (d). e) SHG spectra of the BN monolayer and rBN film (≈1.6 μm thick) under 800 nm excitation. The SHG intensity of rBN can be dramatically enhanced by $\approx 10^7$ times compared with that of the monolayer. f) Excitation power dependence of SHG for monolayer BN and rBN films. The maximum SHG conversion efficiency of the rBN film is determined to be ≈1% with a coherence thickness of 1.6 μm. g) Demonstration of SHG from our rBN nonlinear crystal. Here, the SHG wavelength of 532 nm (with an excitation wavelength of 1064 nm) is chosen specifically for better visualization. h) Comparison of the SHG conversion efficiency of rBN crystalline films to some most representative 2D nonlinear optical crystals reported recently, including quantum dots coated MoS_2 (QD/MoS_2),[16] 3R MoS_2 bulk,[51] ferroelectric $NbOI_2$ and its wrinkled area (W. $NbOI_2$).[50]

different wavelengths (Figure 4g; and Figure S5, Supporting Information). Note that a 1064 nm fundamental wavelength (generating the second-harmonic signals at 532 nm) was specifically chosen for better visualization in Figure 4g. To the best of our knowledge, this represents a recorded value that has ever been reported within the entire 2D material family[44–52] (Figure 4h; and Table S1, Supporting Information).

To further enhance the SHG response of rBN crystalline films, optical phase-matching is a prerequisite for balancing out the wavevector mismatch. In reference to the mature design of conventional nonlinear optical crystals, quasi-phase-matching (QPM) is one of the widely used routes.[53–57] Considering its van der Waals interlayer interaction and atomically flat interfaces, rBN can be artificially stacked to periodically assign the SHG polarization of each film, achieving the QPM for the nearly quadratic augmentation of SHG intensity with the increased number of component films (Note S3, Supporting Information). Furthermore, we fabricated a twist rBN crystal through a well-controlled dry-transfer technique and then measured the SHG intensities of stacked rBN structures (Figure S6, Supporting Information). The SHG signals in the 180°-stacked two-piece and three-piece rBN films (with thickness of ≈1.6 μm for each film) were enhanced by 3.7 and 8.5 times, respectively, as expected. In contrast, the intensity of the 0°-stacked rBN structures showed the sinusoidal oscillation. Our experimental findings are consistent with the theoretical calculations, providing strong demonstration for the QPM process. As a result, through rational design and atomic manufacturing of rBN crystalline films, it is highly desired to reach the practical criterion of ultrathin nonlinear optical crystal.

3. Conclusion

We have proposed a stacking-controlled continuous precipitation strategy to successfully synthesize large-scale rBN crystalline films on single-crystal FeNi vicinal surfaces. The parallel ABC stacking sequence between adjacent layers is unambiguously demonstrated through planar and cross-sectional characterizations. This well-ordered stacking structure ensures the coherent superposition of the SHG polarization of each BN layer, and gives rise to the giant nonlinear frequency conversion efficiency up to 1% within ≈1.6 μm. This work opens a route for the develop-

ment of 2D-material-based miniaturized high-power lasers and compact quantum photonic devices in the future.

4. Experimental Section

Annealing of Single-Crystal FeNi v-(111) Foils: A commercial polycrystalline Permalloy foil (60 wt% Fe, #4J36, Xi'an Gangyan Special Alloy Co. Ltd) was placed on an Al_2O_3 plate and loaded into a tube furnace with a chamber diameter of 6 cm (Hefei Kejing Co. Ltd). The foil was heated to 1450 °C near the molten point in 3 h and kept for 10 h to obtain the single-crystal FeNi v-(111) foil. The system was kept at atmospheric pressure with a mixed gas flow (500 sccm Ar and 50 sccm H_2; sccm means standard cubic centimeter per minute) during the whole process.

Growth of rBN Crystalline Films: The preannealed FeNi v-(111) foil was tightly placed onto the hot-pressed BN paper (90 µm thick, Guangdong Suqun New Material Co. Ltd) on the Al_2O_3 plate and then loaded into the tube furnace. The furnace was heated to 1250 °C in 2 h and maintained for 2–60 h at atmospheric pressure under the mixed flux of N_2 (500 sccm), Ar (100 sccm), and H_2 (50 sccm) to grow rBN crystalline films with different thicknesses. After growth, the system was naturally cooled down to room temperature.

Transfer of rBN Crystalline Films: A typical wet method was used for transferring rBN films for characterization, in which rBN/FeNi samples were first floated on the surface of $FeCl_3$ solution for 10 h to remove the Fe and Ni, then rinsed with deionized water several times and finally placed onto target substrates. Besides, the rBN flakes can be directly exfoliated from the surface of rBN/FeNi samples and released onto substrates using the Scotch tape method. The stacked rBN films for quasiphase-matching measurements were fabricated through a well-controlled dry-transfer technique. A polypropylene carbonate (PPC) film was first spin-coated on a poly(dimethylsiloxane) (PDMS) stamp to pick up one rBN film. Then the system was accurately rotated with 0° (for phase-mismatching) or 180° (for quasiphase-matching), which was controlled by a commercial 2D-material rotary transfer stage (JOOIN Technology, 2DT-7-300). The rBN/PPC film was further stacked onto another rBN on the fused silica and detached from the stamp by heating it at 130 °C. After completely releasing, the stacked rBN films were annealed at 500 °C for 8 h under a low-pressure condition (<200 Pa) with Ar (500 sccm) and H_2 (50 sccm), in order to remove the PPC residue and exclude the interlayer air bubbles.

SHG Measurements: A titanium–sapphire oscillator (Coherent Mira-HP, ≈130 fs, 76 MHz) equipped with an optical parametric oscillator (Coherent Mira-OPO-X, 200 fs, 76 MHz) was used for SHG measurements (if not specified, the wavelength of the fundamental wave was fixed at 800 nm). The excitation laser was focused on the sample with signal collected in an objective-sample-objective confocal transmission configuration. Subsequently, a spectrometer (Princeton SP2500) with a silicon charge coupled device camera was used to record the signal. In order to determine the nonlinear coefficient of rBN, the SHG spectra of commercial *z*-cut $LiNbO_3$ film (thickness of 300 nm) and rBN film (thickness of 730 nm) were simultaneously measured under the 1064 nm laser excitation. To accurately obtain the SHG conversion efficiency, the power of the excitation light ($P(\omega)$) and signal light ($P(2\omega)$) separately was measured. Then the SHG conversion efficiency was calculated as $\eta_{SHG} = P(2\omega)/P(\omega)$, taking the transmission loss into account. Since $P = I \cdot A$, where A represents the spot area, the efficiency can be also expressed as $I(2\omega)/I(\omega)$. Polarized SHG pattern measurements were performed by adding a half-wave plate in front of the focusing objective in a reflection geometry.

SHG Simulations: The NumPy scientific computing package in Spyder (Python 3.7) was used for all SHG simulations. To describe the interaction between the fundamental and SHG signals, nonlinear coupled-wave equations were employed. And the refractive index of BN at different wavelengths was obtained from the Sellmeier equation.

Characterizations: Raman spectrum was obtained at room temperature using SmartRaman confocal-micro-Raman module (Institute of Semiconductors, Chinese Academy of Sciences) with an incident light wavelength of 532 nm. UV–vis spectral measurement was performed using a Varian Cary 5000 NIR–vis–UV spectrophotometer. XRD 2θ-scan and φ-scan measurements were performed using a Bruker D8 Discover system and a X'Pert^3 MRD system, respectively. XPS was performed using Axis Ultra Imaging X-ray photoelectron spectrometer. AFM mappings were obtained by a Bruker Dimensional ICON system at ambient atmosphere. SEM and EDS images were collected by an FEI Nova NanoSEM 430 scanning electron microscope equipped with Ultim max 100 nanoprobe. EBSD mappings were performed using a PHI 710 scanning Auger nanoprobe. HRTEM, SAED, and STEM experiments were obtained in FEI Titan Themis G2 300 operated at 300 kV.

Supporting Information

Supporting Information is available from the Wiley Online Library or from the author.

Acknowledgements

J.Q., C.M., Q.G., and C.M. contributed equally to this work. This work was supported by the National Key R&D Program of China (Nos. 2022YFA1403500 and 2022YFA1405600), National Natural Science Foundation of China (Nos. 52025023, 51991342, 52021006, 92163206, 11888101, T2188101, and 12104018), Guangdong Major Project of Basic and Applied Basic Research (No. 2021B0301030002), the Strategic Priority Research Program of Chinese Academy of Sciences (No. XDB33000000).

Conflict of Interest

The authors declare no conflict of interest.

Data Availability Statement

The data that support the findings of this study are available from the corresponding author upon reasonable request.

Keywords

2D materials, nonlinear optical crystals, rhombohedral boron nitride, second-harmonic generation

Received: April 4, 2023
Revised: July 3, 2023
Published online:

[1] Y. Kubota, K. Watanabe, O. Tsuda, T. Taniguchi, *Science* **2007**, *317*, 932.
[2] G. Cassabois, P. Valvin, B. Gil, *Nat. Photonics* **2016**, *10*, 262.
[3] Y. L. Li, Y. Rao, K. F. Mak, Y. M. You, S. Y. Wang, C. R. Dean, T. F. Heinz, *Nano Lett.* **2013**, *13*, 3329.
[4] C. J. Kim, L. Brown, M. W. Graham, R. Hovden, R. W. Havener, P. L. McEuen, D. A. Muller, J. Park, *Nano Lett.* **2013**, *13*, 5660.
[5] H. Wang, X. Qian, *Nano Lett.* **2017**, *17*, 5027.
[6] A. Autere, H. Jussila, Y. Y. Dai, Y. D. Wang, H. Lipsanen, Z. P. Sun, *Adv. Mater.* **2018**, *30*, 1705963.
[7] T. Stiehm, R. Schneider, J. Kern, I. Niehues, S. M. de Vasconcellos, R. Bratschitsch, *Rev. Sci. Instrum.* **2019**, *90*, 083102.
[8] S. Kim, J. E. Froch, A. Gardner, C. Li, I. Aharonovich, A. S. Solntsev, *Opt. Lett.* **2019**, *44*, 5792.

[9] Z. Liu, Y. J. Gong, W. Zhou, L. L. Ma, J. J. Yu, J. C. Idrobo, J. Jung, A. H. MacDonald, R. Vajtai, J. Lou, P. M. Ajayan, *Nat. Commun.* **2013**, *4*, 2541.
[10] N. Tancogne-Dejean, A. Rubio, *Sci. Adv.* **2018**, *4*, eaao5207.
[11] J. D. Caldwell, I. Aharonovich, G. Cassabois, J. H. Edgar, B. Gil, D. N. Basov, *Nat. Rev. Mater.* **2019**, *4*, 552.
[12] A. Rousseau, P. Valvin, W. Desrat, L. J. Xue, J. H. Li, J. H. Edgar, G. Cassabois, B. Gil, *ACS Nano* **2022**, *16*, 2756.
[13] S. Moon, J. Kim, J. Park, S. Im, J. Kim, I. Hwang, J. K. Kim, *Adv. Mater.* **2023**, *35*, 2204161.
[14] Y. Zhao, J. Ye, H. Wang, F. Zhang, M. H. Sun, B. H. Yu, J. L. Wang, Y. Liu, X. Y. Shan, X. D. Bai, W. L. Wang, *J. Phys. Chem. Lett.* **2021**, *12*, 9475.
[15] K. Y. Yao, N. R. Finney, J. Zhang, S. L. Moore, L. D. Xian, N. Tancogne-Dejean, F. Liu, J. Ardelean, X. Y. Xu, D. Halbertal, K. Watanabe, T. Taniguchi, H. Ochoa, A. Asenjo-Garcia, X. Y. Zhu, D. N. Basov, A. Rubio, C. R. Dean, J. Hone, P. J. Schuck, *Sci. Adv.* **2021**, *7*, eabe8691.
[16] H. Hong, C. C. Wu, Z. X. Zhao, Y. G. Zuo, J. H. Wang, C. Liu, J. Zhang, F. F. Wang, J. G. Feng, H. B. Shen, J. B. Yin, Y. C. Wu, Y. Zhao, K. H. Liu, P. Gao, S. Meng, S. W. Wu, Z. P. Sun, K. H. Liu, J. Xiong, *Nat. Photonics* **2021**, *15*, 510.
[17] J. S. Lee, S. H. Choi, S. J. Yun, Y. I. Kim, S. Boandoh, J. H. Park, B. G. Shin, H. Ko, S. H. Lee, Y. M. Kim, Y. H. Lee, K. K. Kim, S. M. Kim, *Science* **2018**, *362*, 817.
[18] L. Wang, X. Z. Xu, L. N. Zhang, R. X. Qiao, M. H. Wu, Z. C. Wang, S. Zhang, J. Liang, Z. H. Zhang, Z. B. Zhang, W. Chen, X. D. Xie, J. Y. Zong, Y. W. Shan, Y. Guo, M. Willinger, H. Wu, Q. Y. Li, W. L. Wang, P. Gao, S. W. Wu, Y. Zhang, Y. Jiang, D. P. Yu, E. G. Wang, X. D. Bai, Z. J. Wang, F. Ding, K. H. Liu, *Nature* **2019**, *570*, 91.
[19] T. A. Chen, C. P. Chuu, C. C. Tseng, C. K. Wen, H. S. P. Wong, S. Y. Pan, R. T. Li, T. A. Chao, W. C. Chueh, Y. F. Zhang, Q. Fu, B. I. Yakobson, W. H. Chang, L. J. Li, *Nature* **2020**, *579*, 219.
[20] K. Y. Ma, L. Zhang, S. Jin, Y. Wang, S. I. Yoon, H. Hwang, J. Oh, D. Jeong, M. Wang, S. Chatterjee, G. Kim, A. R. Jang, J. Yang, S. Ryu, H. Y. Jeong, R. S. Ruoff, M. Chhowalla, F. Ding, H. S. Shin, *Nature* **2022**, *606*, 88.
[21] L. Xu, J. Zhan, J. Hu, Y. Bando, X. Yuan, T. Sekiguchi, M. Mitome, D. Golberg, *Adv. Mater.* **2007**, *19*, 2141.
[22] M. Chubarov, H. Pedersen, H. Högberg, J. Jensen, A. Henry, *Cryst. Growth Des.* **2012**, *12*, 3215.
[23] M. Moret, A. Rousseau, P. Valvin, S. Sharma, L. Souqui, H. Pedersen, H. Högberg, G. Cassabois, J. Li, J. Edgar, *Appl. Phys. Lett.* **2021**, *119*, 262102.
[24] L. Song, L. J. Ci, H. Lu, P. B. Sorokin, C. H. Jin, J. Ni, A. G. Kvashnin, D. G. Kvashnin, J. Lou, B. I. Yakobson, P. M. Ajayan, *Nano Lett.* **2010**, *10*, 3209.
[25] Y. M. Shi, C. Hamsen, X. T. Jia, K. K. Kim, A. Reina, M. Hofmann, A. L. Hsu, K. Zhang, H. N. Li, Z. Y. Juang, M. S. Dresselhaus, L. J. Li, J. Kong, *Nano Lett.* **2010**, *10*, 4134.
[26] Y. Gao, W. C. Ren, T. Ma, Z. B. Liu, Y. Zhang, W. B. Liu, L. P. Ma, X. L. Ma, H. M. Cheng, *ACS Nano* **2013**, *7*, 5199.
[27] P. Sutter, J. Lahiri, P. Zahl, B. Wang, E. Sutter, *Nano Lett.* **2013**, *13*, 276.
[28] J. D. Li, Y. Li, J. Yin, X. B. Ren, X. F. Liu, C. H. Jin, W. L. Guo, *Small* **2016**, *12*, 3645.
[29] K. Watanabe, T. Taniguchi, H. Kanda, *Nat. Mater.* **2004**, *3*, 404.
[30] C. H. Zhang, L. Fu, S. L. Zhao, Y. Zhou, H. L. Peng, Z. F. Liu, *Adv. Mater.* **2014**, *26*, 1776.
[31] S. M. Kim, A. Hsu, M. H. Park, S. H. Chae, S. J. Yun, J. S. Lee, D. H. Cho, W. J. Fang, C. Lee, T. Palacios, M. Dresselhaus, K. K. Kim, Y. H. Lee, J. Kong, *Nat. Commun.* **2015**, *6*, 8662.
[32] Z. Y. Shi, X. J. Wang, Q. T. Li, P. Yang, G. Y. Lu, R. Jiang, H. S. Wang, C. Zhang, C. X. Cong, Z. Liu, T. R. Wu, H. M. Wang, Q. K. Yu, X. M. Xie, *Nat. Commun.* **2020**, *11*, 849.
[33] J. Li, J. Wang, X. Zhang, C. Elias, G. Ye, D. Evans, G. Eda, J. M. Redwing, G. Cassabois, B. Gil, P. Valvin, R. He, B. Liu, J. H. Edgar, *ACS Nano* **2021**, *15*, 7032.
[34] S. Fukamachi, P. Solís-Fernández, K. Kawahara, D. Tanaka, T. Otake, Y.-C. Lin, K. Suenaga, H. Ago, *Nat. Electron.* **2023**, *6*, 126.
[35] G. Constantinescu, A. Kuc, T. Heine, *Phys. Rev. Lett.* **2013**, *111*, 036104.
[36] C. Cazorla, T. Gould, *Sci. Adv.* **2019**, *5*, eaau5832.
[37] Y. Uchida, S. Nakandakari, K. Kawahara, S. Yamasaki, M. Mitsuhara, H. Ago, *ACS Nano* **2018**, *12*, 6236.
[38] M. H. Wu, Z. B. Zhang, X. Z. Xu, Z. H. Zhang, Y. R. Duan, J. C. Dong, R. X. Qiao, S. F. You, L. Wang, J. J. Qi, D. X. Zou, N. Z. Shang, Y. B. Yang, H. Li, L. Zhu, J. L. Sun, H. J. Yu, P. Gao, X. D. Bai, Y. Jiang, Z. J. Wang, F. Ding, D. P. Yu, E. G. Wang, K. H. Liu, *Nature* **2020**, *581*, 406.
[39] Z. Zhang, M. Ding, T. Cheng, R. Qiao, M. Zhao, M. Luo, E. Wang, Y. Sun, S. Zhang, X. Li, Z. Zhang, H. Mao, F. Liu, Y. Fu, K. Liu, D. Zou, C. Liu, M. Wu, C. Fan, X. Wang, P. Gao, Q. Li, K. Liu, Y. Zhang, X. Bai, D. Yu, F. Ding, E. Wang, K. Liu, *Nat. Nanotechnol.* **2022**, *17*, 1258.
[40] Q. R. Cai, D. Scullion, W. Gan, A. Falin, S. Y. Zhang, K. Watanabe, T. Taniguchi, Y. Chen, E. J. G. Santos, L. H. Li, *Sci. Adv.* **2019**, *5*, eaav0129.
[41] A. Rousseau, M. Moret, P. Valvin, W. Desrat, J. H. Li, E. Janzen, L. J. Xue, J. H. Edgar, G. Cassabois, B. Gil, *Phys. Rev. Mater.* **2021**, *5*, 262102.
[42] S. M. Gilbert, T. Pham, M. Dogan, S. Oh, B. Shevitski, G. Schumm, S. Liu, P. Ercius, S. Aloni, M. L. Cohen, A. Zettl, *2D Mater.* **2019**, *6*, 021006.
[43] S. Y. Lee, T. Y. Jeong, S. Jung, K. J. Yee, *Phys. Status Solidi B* **2019**, *256*, 1800417.
[44] K. L. Seyler, J. R. Schaibley, P. Gong, P. Rivera, A. M. Jones, S. F. Wu, J. Q. Yan, D. G. Mandrus, W. Yao, X. D. Xu, *Nat. Nanotechnol.* **2015**, *10*, 407.
[45] M. Zhao, Z. L. Ye, R. Suzuki, Y. Ye, H. Y. Zhu, J. Xiao, Y. Wang, Y. Iwasa, X. Zhang, *Light: Sci. Appl.* **2016**, *5*, e16131.
[46] J. Shi, P. Yu, F. C. Liu, P. He, R. Wang, L. Qin, J. B. Zhou, X. Li, J. D. Zhou, X. Y. Sui, S. Zhang, Y. F. Zhang, Q. Zhang, T. C. Sum, X. H. Qiu, Z. Liu, X. F. Liu, *Adv. Mater.* **2017**, *29*, 1701486.
[47] X. P. Fan, Y. Jiang, X. J. Zhuang, H. J. Liu, T. Xu, W. H. Zheng, P. Fan, H. L. Li, X. P. Wu, X. L. Zhu, Q. L. Zhang, H. Zhou, W. Hu, X. Wang, L. T. Sun, X. F. Duan, A. L. Pan, *ACS Nano* **2017**, *11*, 4892.
[48] X. Wen, Z. Gong, D. Li, *InfoMat* **2019**, *1*, 317.
[49] J. Yu, X. F. Kuang, J. Z. Li, J. H. Zhong, C. Zeng, L. K. Cao, Z. W. Liu, Z. X. S. Zeng, Z. Y. Luo, T. C. He, A. L. Pan, Y. P. Liu, *Nat. Commun.* **2021**, *12*, 1083.
[50] I. Abdelwahab, B. Tilmann, Y. Z. Wu, D. Giovanni, I. Verzhbitskiy, M. L. Zhu, R. Berte, F. Y. Xuan, L. D. Menezes, G. Eda, T. C. Sum, S. Y. Quek, S. A. Maier, K. P. Loh, *Nat. Photonics* **2022**, *16*, 644.
[51] X. Y. Xu, C. Trovatello, F. Mooshammer, Y. M. Shao, S. Zhang, K. Y. Yao, D. N. Basov, G. Cerullo, P. J. Schuck, *Nat. Photonics* **2022**, *16*, 698.
[52] Q. Guo, X. Z. Qi, L. Zhang, M. Gao, S. Hu, W. Zhou, W. Zang, X. Zhao, J. Wang, B. Yan, M. Xu, Y. K. Wu, G. Eda, Z. Xiao, S. A. Yang, H. Gou, Y. P. Feng, G. C. Guo, W. Zhou, X. F. Ren, C. W. Qiu, S. J. Pennycook, A. T. S. Wee, *Nature* **2023**, *613*, 53.
[53] N. Bloembergen, *Nonlinear Optics*, World Scientific, Singapore **1992**.
[54] S. Zhu, Y. Y. Zhu, N. B. Ming, *Science* **1997**, *278*, 843.
[55] G. G. Gurzadyan, V. G. Dmitriev, D. N. Nikogosyan, *Handbook of Nonlinear Optical Crystals*, Springer, New York **1999**.
[56] Y. R. Shen, *The Principles of Nonlinear Optics*, Wiley-VCH, Weinheim, Germany **2003**.
[57] R. W. Boyd, *Nonlinear Optics*, Academic Press, London, UK **2008**.